EXPLORING THE ASYMMETRIC MOMENTUM ACCEPTANCE AT THE CERN SUPER PROTON SYNCHROTRON

L. Pauwels*,[1,2], H. Bartosik[1], M. Hostettler[1], G. Iadarola[1], N. Pauly[2],
F. F. Van der Veken[1], J. Wenninger[1]
[1]CERN, Meyrin, Switzerland,
[2]Université Libre de Bruxelles, Brussels, Belgium

Abstract

Studies conducted at CERN's Super Proton Synchrotron (SPS) in 2017 showed an asymmetric off-momentum acceptance for Q20 optics. A systematic mechanical limitation near the defocussing quadrupoles, the most restrictive regions of the ring in the Q20 optics, was suggested as a possible explanation for this asymmetry and was addressed during LS2. However, improvements were only observed in some of those locations. This paper aims to revisit this topic to identify potential bottlenecks and their causes. Additionally, some regions are more limiting than others despite having the same linear optics, which could be explained by aperture shifts, orbit misalignments, non-linear contributions of the lattice, or any combination of those. Measurements were performed at different locations by introducing orbit bumps and changing the frequency of the RF cavities, in order to identify the dominant bottleneck regions. In parallel, simulations were conducted to predict the location of the primary bottleneck and to reproduce the experimental data.

INTRODUCTION

The Super Proton Synchrotron (SPS) at CERN is the final stage of the Large Hadron Collider (LHC) injection chain, accelerating particles from 26 GeV to 450 GeV with an intensity up to $2.6 \cdot 10^{11}$ protons per bunch [1]. Keeping losses within the required threshold is crucial at this stage to ensure efficient transfer of these high-intensity beams to the LHC, while limiting operational downtime and activation of the SPS [2]. A key parameter in managing losses is the momentum acceptance of a machine, defined as the range of relative momentum deviations $\delta = \frac{\Delta P}{p}$ for which particles remain stably confined in the machine, limited by the transverse aperture of dispersive elements [3]. A measurement campaign led in 2017 showed that this parameter was asymmetric for the SPS: the negative momentum acceptance is significantly smaller than the positive one. A possible explanation was the presence of asymmetric apertures near the machine's defocusing quadrupoles. These were replaced during the second long shutdown (LS2), but only a partial improvement was observed in said loss locations [4–6].

Measurements performed in June 2025 confirmed that the asymmetry persists. Scans at different normalised chromaticities ($\xi = \frac{Q'}{Q}$) reveal a clear dependence on the negative side, while the positive side remains unchanged, as shown in Fig. 1. These observations indicate that the reduced negative momentum acceptance cannot be attributed solely to mechanical aperture limitations, but instead point to a beam-dynamics origin.

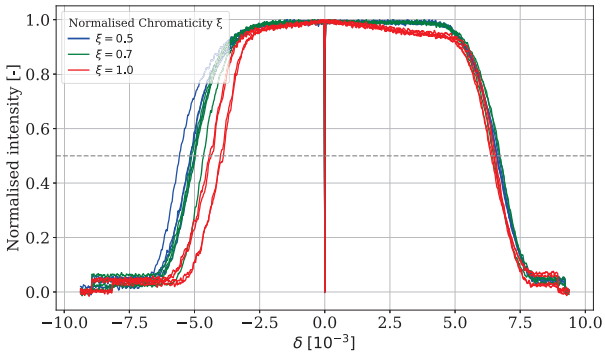

Figure 1: Normalised intensity vs. δ measured in June 2025 for three values of normalised chromaticity ξ. A chromaticity dependence is observed only on the negative side.

This paper presents a systematic study of the asymmetric momentum acceptance in the SPS. An extensive measurement campaign, guided by optics considerations and building on the 2017 observations, was carried out to identify potential bottleneck regions through combined orbit-bump and momentum-displacement scans. The measurements allow the identification of the dominant limiting locations responsible for the asymmetry. The results are then compared with tracking simulations reproducing the experimental conditions, with the aim of gaining insight into the underlying beam-dynamics origin and its chromaticity dependence.

MEASUREMENTS STRATEGY AND OPTICS CONTEXT

The momentum acceptance is probed by means of a radio-frequency sweep (RF-sweep), in which the cavity frequency is varied to shift the central momentum of the beam. In a first-order approximation, the frequency deviation required to generate a momentum offset δ is given by:

$$\frac{\Delta f}{f_0} = -\eta \delta \tag{1}$$

where f_0 is the nominal RF-frequency of the cavities, $\eta = \alpha_c - \frac{1}{\gamma^2}$ is the slip factor with α_c the momentum compaction factor and $\delta = \frac{\Delta p}{p}$ the relative momentum deviation [3, 7]. The resulting momentum offset displaces the closed orbit transversely through dispersion, with a shift $\Delta x = D\delta$ where x is the horizontal transverse position of the beam at a certain

* lise.eliane.pauwels@cern.ch

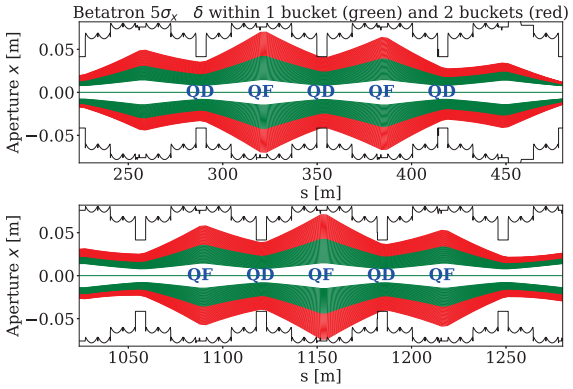

Figure 2: Horizontal beam envelope for betatron oscillations at $5\sigma_x$ and momentum deviations within one (green) and two (red) bucket heights, shown for dispersion waves around a QD (upper) and a QF (lower). In black are the physical apertures, including a correction for the effect of the beam sagitta in the main dipoles [9].

position and $D(s)$ the local dispersion function. In high dispersion regions, this shift can push the beam onto the aperture if the induced momentum offset is large enough.

The SPS lattice has a 6-fold symmetry, which modulates the dispersion function around the ring and creates regions of alternating high and low dispersion. For the Q20 optics (used for LHC-type beams [8]), this results in 18 dispersion waves, each centred on either a QF-QD-QF or a QD-QF-QD sequence–QF being the focusing quadrupoles and QD the defocusing ones. Since off-momentum particles undergo a dispersive closed orbit shift proportional to the local dispersion, the centres of these waves are where the beam excursion is largest and therefore where aperture limitations are most likely to occur. While the dispersion reaches its maximum at the QF locations (up to 7 m), their significantly larger chamber means the beam excursion remains within acceptable limits. The QDs, despite lower dispersion, have considerably more restrictive apertures, making them the primary bottleneck candidates. However, since the QFs approach the aperture limit as well, all candidate elements in high-dispersion regions were included in the scan campaign, as illustrated in Fig. 2.

To experimentally identify and rank these bottlenecks, a dedicated scan campaign was conducted. At each candidate element, a local closed orbit bump of increasing amplitude was introduced prior to an RF-sweep. The 50% intensity loss threshold was chosen as a common figure of merit to allow direct comparison between bottlenecks: an element at which this threshold is reached for smaller δ and smaller bump amplitude is identified as more limiting. The independence of the results on beam intensity and transverse emittance was verified experimentally, confirming the reproducibility of the measurements.

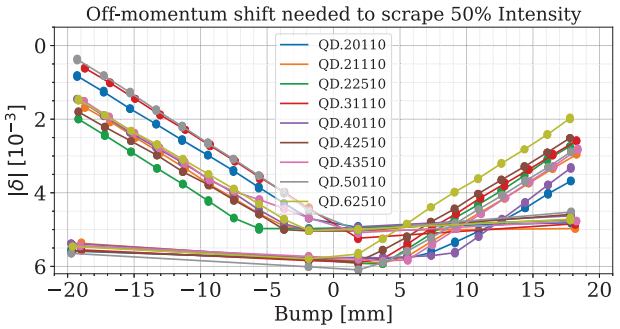

Figure 3: Measured 50% intensity loss threshold as a function of bump amplitude for the most limiting bottlenecks.

BOTTLENECK IDENTIFICATION

All candidate bottlenecks, namely all focusing and defocusing quadrupoles at the centre of each dispersion wave, were scanned during machine development sessions. For each element, the δ at which 50% intensity loss occurs was recorded as a function of bump amplitude. Orbit bumps were primarily applied with the same sign as the momentum sweep to enhance the beam excursion at the candidate bottleneck. A small number of opposite-sign bumps were additionally performed to evaluate whether displacing the beam away from it improves the loss situation. Figure 3 shows the results for the most limiting elements. As the bump amplitude increases, the local aperture at the scanned element is progressively reduced, and the loss threshold shifts to smaller $|\delta|$. Elements for which this shift occurs at small bump amplitudes are identified as the most limiting bottlenecks, as they constrain the momentum acceptance even under modest aperture perturbations. A clear separation between curves is observed, revealing a hierarchy among the candidate elements. Consistent with the optics analysis, all main bottlenecks are defocusing quadrupoles QD, found in both QF-QD-QF and QD-QF-QD wave types. Among these, three elements, QD.20110, QD.31110 and QD.50110, stand out as particularly limiting, reaching the loss threshold at significantly smaller $|\delta|$ and bump amplitudes than the others. Furthermore, the scan directly captures the asymmetry observed in the RF-sweep measurements: for negative off-momentum, the loss threshold is reached at smaller $|\delta|$ and for smaller bump amplitudes than on the positive side.

COMPARISON WITH SIMULATION

The measurements presented in the previous section are compared with particle tracking simulations performed with Xsuite [10], using an updated optics model of the SPS [9]. Simulated RF-sweep loss curves, coded with Xcoll [11], are shown alongside measurements in Fig. 4. While the simulation predicts a larger momentum acceptance on both sides, the chromaticity dependence on the negative side is qualitatively reproduced: higher chromaticity leads to a more restrictive negative acceptance, with no such dependence on the positive side. Since a purely mechanical aperture limitation would be insensitive to chromaticity, this agreement

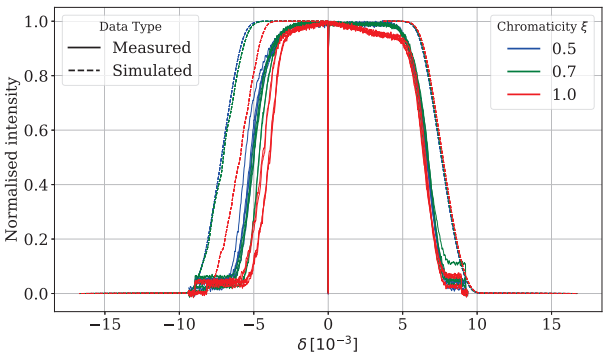

Figure 4: Normalised intensity vs. δ for three chromaticity values, comparing simulation (dashed) and experiment (solid).

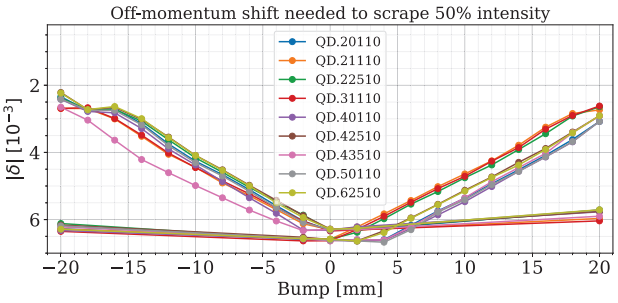

Figure 5: Simulated 50% intensity loss threshold as a function of bump amplitude for all candidate bottlenecks.

strongly suggests a beam dynamics origin for the asymmetry and validates the use of simulation as a tool to investigate it.

To assess whether the simulation identifies the correct limiting elements, the bump-scan procedure was reproduced numerically for all candidate bottlenecks, both QFs and QDs of the dispersion waves. The resulting main midpoint curves are shown in Fig. 5. As in the experiment, QFs are never found to be limiting: all restrictive elements are QDs, confirming that this conclusion is not an artefact of the measurement conditions but is reproduced by the model. The spread between locations is however considerably less pronounced in simulation, with most QDs clustering closely together, whereas the experiment shows a clearer hierarchy.

A direct comparison of the three most limiting elements, QD.20110, QD.31110, and QD.50110, is shown in Fig 6. The acceptance is overestimated on both sides, and the asymmetry between the negative and positive sides is less pronounced in simulation. The three elements are only marginally more restrictive than the other QDs in simulation, and their relative ranking is not fully preserved. In particular, QD.31110 stands out on the positive side, where the measured acceptance is significantly closer to the simulated value than for the other two elements. Nevertheless, the same locations are consistently identified as among the most limiting, and together with the reproduced chromaticity dependence, this gives confidence that the simulation captures the relevant loss mechanism and can be used to guide further studies of the asymmetry.

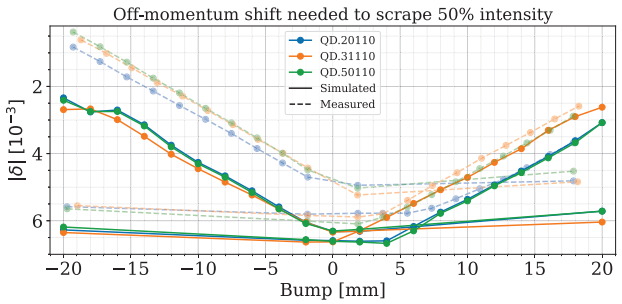

Figure 6: Comparison of simulated (solid) and measured (dashed) 50% intensity loss thresholds as a function of bump amplitude for the three most limiting elements.

CONCLUSION

A systematic study of the asymmetric momentum acceptance in the SPS Q20 optics has been presented. Combined orbit-bump and RF-sweep scans across all candidate bottleneck regions of the 18 dispersion waves consistently identified defocusing quadrupoles as the dominant limiting elements, with QD.20110, QD.31110 and QD.50110 standing out as the most restrictive. The asymmetry between negative and positive momentum acceptance is directly captured in the bump scans, with the negative side reaching the loss threshold at significantly smaller $|\delta|$ and bump amplitudes. Particle tracking simulations with Xsuite qualitatively reproduce both the chromaticity dependence of the negative acceptance and the identification of the same limiting locations, supporting the interpretation of a beam dynamics contribution to the observed asymmetry. Quantitative discrepancies remain, with the simulation overestimating the acceptance on both sides and showing a less pronounced hierarchy among bottlenecks. These results establish a simulation framework that provides a consistent description of the observations, although quantitative discrepancies remain. The impact of magnetic errors on the simulated acceptance will be explored in future studies, as a more realistic machine description may help bridge the gap with the experimental data. The chromaticity dependence of the negative acceptance, observed both in experiment and simulation, further motivates a dedicated investigation of the tune evolution during the RF-sweep, to assess whether resonance crossing may contribute to the observed losses.

REFERENCES

[1] J. Coupard *et al.*, 'LHC Injectors Upgrade, Technical Design Report, Vol. I: Protons', CERN, Geneva, Switzerland, Rep. CERN-ACC-2014-0337, 2014. doi:10.17181/CERN.7NHR.6HGC

[2] G. Rumolo *et al.*, 'Beam Performance with the LHC Injectors Upgrade', in *Proc. HB'23*, Geneva, Switzerland, Oct. 2023, pp. 1–8. doi:10.18429/JACoW-HB2023-MOA1I1

[3] H. Wiedemann, *Particle accelerator physics*. Springer, 2007.

[4] F. M. Velotti *et al.*, 'SPS quadrupole dog-leg and alignment post LS2', 2019. https://cds.cern.ch/record/2673270

[5] V. Kain *et al.*, 'Identification and Removal of SPS Aperture Limitations', in *Proc. IPAC'18*, Vancouver, Canada, Apr.-May 2018, pp. 709–712. doi:10.18429/JACoW-IPAC2018-TUPAF021

[6] V. Kain, H. Bartosik, S. C. Cave, K. Cornelis and F. M. Velotti, 'Automatic Local Aperture Measurements in the SPS', in *Proc. IPAC'17*, Copenhagen, Denmark, May 2017, pp. 4073–4076. doi:10.18429/JACoW-IPAC2017-THPAB147

[7] S. Y. Lee, *Accelerator physics*. World Scientific, 1999.

[8] Y. Papaphilippou *et al.*, 'Operational performance of the lhc proton beams with the sps low transition energy optics', 2013. https://cds.cern.ch/record/1581446

[9] L. Pauwels *et al.*, 'Modelling Beam Losses in CERN's Super Proton Synchrotron With Xsuite', paper presented at the 17th International Particle Accelerator Conf. (IPAC'26), Deauville, France, May 2026, paper THP4103, this conference.

[10] G. Iadarola *et al.*, 'Xsuite: an integrated beam physics simulation framework', in *Proc. HB'23*, Geneva, Switzerland, Oct. 2023, pp. 73–80. doi:10.18429/JACoW-HB2023-TUA2I1

[11] F. Van der Veken *et al.*, 'Recent Developments with the New Tools for Collimation Simulations in Xsuite', in *Proc. HB'23*, Geneva, Switzerland, Oct. 2023, pp. 474–478. doi:10.18429/JACoW-HB2023-THBP13